metals

MDPI

Article

A Characterization of the Powder Yield Behaviors During a Hot Isostatic Pressing Process

Guozheng Quan [1,2,*], Wenjing Ran [1], Weiwei Dai [2], Qian Jiang [2], Yanze Yu [1] and Yu Zhang [1]

[1] Chongqing Key Laboratory of Advanced Mold Intelligent Manufacturing, School of Material Science and Engineering, Chongqing University, Chongqing 400044, China
[2] Jiangsu Advanced Manufacturing Engineering Technology Research Center for Marine Power System Parts, COSCO Shipping Marine Equipment & Spares (Nanjing) Co., Ltd., Nanjing 211121, China; dai.weiwei@coscoshipping.com (W.D.); jiang.qian1@coscoshipping.com (Q.J.)
* Correspondence: quanguozheng@cqu.edu.cn; Tel.: +86-15922900904

Abstract

The constitutive model significantly influences the accuracy of predicting the complex rheological behavior of hot isostatically pressed powders. The temperature plays a crucial role in determining material properties during hot isostatic pressing (HIP), making it essential to account for its effect on the yield model parameters to more accurately describe the densification evolution of powders. In this study, HIP experiments were conducted using two different process schemes, and the shrinkage deformation of the envelope under each scheme was analyzed. High-temperature uniaxial compression experiments were performed on HIP samples with varying densities to analyze and characterize the stress–strain response of the powder during HIP. A mesoscopic particle-scale high-temperature uniaxial compression model was developed based on the discrete element method (DEM), and the strain and stress values corresponding to different densities in the high-temperature uniaxial compression simulations were validated through experimental comparison. The strain evolution during the uniaxial compression process was analyzed, and the relationship between the parameters of the Shima–Oyane model and the temperature was established, leading to the development of a temperature-compensated Shima–Oyane model. Based on the obtained parameters at various densities and temperatures, a yield stress map for the nickel-based alloy was constructed. The accuracy of this model was verified by comparing experimental results with finite element method (FEM) simulations. The findings of this study contribute to a more precise prediction of densification behavior in thermally driven isostatic pressing.

Keywords: hot isostatic pressing; nickel-based alloy; powder particle; densification

check for updates

Academic Editors: Andrea Di Schino and Jan Vrestal

Received: 15 May 2025
Revised: 15 June 2025
Accepted: 30 June 2025
Published: 4 July 2025

Citation: Quan, G.; Ran, W.; Dai, W.; Jiang, Q.; Yu, Y.; Zhang, Y. A Characterization of the Powder Yield Behaviors During a Hot Isostatic Pressing Process. *Metals* **2025**, *15*, 752. https://doi.org/10.3390/met15070752

Copyright: © 2025 by the authors. Licensee MDPI, Basel, Switzerland. This article is an open access article distributed under the terms and conditions of the Creative Commons Attribution (CC BY) license (https://creativecommons.org/licenses/by/4.0/).

1. Introduction

Hot isostatic pressing (HIP) is an advanced materials-processing technology. It consolidates powders at high temperatures and pressures to produce fully dense, near-net-shape components. Due to its ability to manufacture isotropic components with excellent mechanical properties, HIP is widely utilized in critical aerospace, biomedical, and energy industries [1–3]. However, the component performance is governed by the complex interplay of thermos–mechanical phenomena, including time–temperature–pressure dependencies, viscoplasticity deformation, and diffusion-driven pore closure [4,5]. These multiscale, interdependent mechanisms occur nonlinearly across varying stages of densification, complicating predictive modeling and optimization. Therefore, different constitutive equations

are used to simulate the flow behavior and densification mechanisms of metal powders during HIP process, such as the power-law creep equation [6,7], Drucker-Prager model [8], the Can-Clay model [8], the Perzyna model [9,10], and the Shima–Oyane model [11,12]. It is worth noting that, although the Shima–Oyane model does not account for key mechanisms in HIP such as diffusional creep, grain boundary diffusion, and pore surface tension effects, it has nonetheless become a widely adopted approach for modeling densification, owing to its broad applicability across a wide density range and its compatibility with various alloy systems. Wang et al. [12] established a HIP densification map using the Shima–Oyane model. Liu's group [13] utilized the Perzyna model to investigate titanium alloy compacts' high-temperature plasticity and creep coupling behavior. Although the Shima–Oyane model is applied to most materials and provides highly accurate predictions across a wide density range, the stresses in these materials are temperature-dependent. Based on the subsequent simulation data and fitting results, it can be seen that the parameter f' in the Shima–Oyane model exhibits an extremely strong temperature dependence. To accurately characterize the density evolution behavior of powders during HIP, the effect of the temperature on the yielding model parameters must be considered.

Since the powder materials cannot be regarded as standard volumetrically compressible continua, significant strain, shrinkage, and deformation occur during the HIP process [14,15]. The continuum model is only suitable for describing the overall shrinkage and deformation of the powder during the HIP process. However, it has limitations in accurately capturing the individual powder particles' motion and deformation behavior. Coupling the finite element method (FEM) with the discrete element method (DEM) enables representation of the powder particle system as a solid continuum deformable body, thereby achieving an accurate description of the powder flow, deformation, and contact behavior. At present, this coupled approach has been successfully applied in the analysis of powder densification mechanisms [16–20], the construction of yield surfaces [21,22], the quantification of friction effects [23,24], and the simulation of compaction processes [25,26]. Elguezabal et al. [27] utilized the model to predict mechanical behavior at the mesoscopic particle scale. Li et al. [28] established various initial packing structures and investigated different densification mechanisms for three powders: single-particle powder, binary powder, and powder with a normal particle size distribution. Zou et al. [29] conducted a numerical reproduction of tungsten powder and examined the effects of the HIP process parameters on its compaction behavior. To this end, it is essential to establish a cross-scale correlation model linking macroscopic mechanical properties with microscopic particle dynamics to elucidate the densification mechanism of powders during HIP, thereby providing theoretical support for process optimization and improving product performance.

In this study, the high-temperature uniaxial compression behavior of powder particles was accurately simulated using a cross-scale coupled FEM-DEM approach, through which a temperature-compensated Shima–Oyane-based model was developed. Firstly, a random stacking structure of Inconel 625 powder was generated using the DEM. Subsequently, a finite element model was introduced for a numerical simulation and analysis. Two different HIP experimental schemes were conducted to evaluate the shrinkage behavior of HIP parts under varying process conditions. High-temperature uniaxial compression experiments and simulations were carried out on HIP parts with different initial densities to systematically investigate and characterize their stress–strain responses during hot extrusion. The simulation results were rigorously validated against experimental data, confirming the accuracy and reliability of the established high-temperature uniaxial compression model. A quantitative relationship between Shima–Oyane model parameters and temperature was identified through integrated simulation and experimental analyses, resulting in the formulation of a temperature-compensated Shima–Oyane constitutive model. This model

was implemented into finite element simulations, and its predictive accuracy was validated through detailed comparisons with experimental observations. Introducing the temperature-compensated Shima–Oyane model significantly deepens the understanding of the powder deformation behavior under HIP conditions and offers robust theoretical insights and guidance for the multi-objective optimization of process parameters.

2. A Solution Approach to Powder Yield Model During HIP Process

2.1. Improved Shima–Oyane Model: Its Solution Approach

Plastic deformation and substantial volume shrinkage occur during the powder HIP process. Since the conventional von Mises yield criterion cannot predict the yield behavior under volume changes, it cannot meet the numerical simulation needs of powder HIP. Therefore, considering the volume change, flow stress, and hydrostatic pressure during powder deformation, Shima et al. [30,31] introduced the effect of hydrostatic pressure and developed an improved yield criterion, from which the effect of volume shrinkage can be predicted. The formula of the yield criterion is as follows [30,31]:

$$F = \sqrt{\frac{1}{2}\left[(\sigma_1-\sigma_2)^2+(\sigma_2-\sigma_3)^2+(\sigma_1-\sigma_3)^2\right]+\left(\frac{\sigma_m}{f}\right)^2} \quad (1)$$

where F is a parameter related to the yield strength of material; σ_1, σ_2, and σ_3 are the first, second, and third principal stresses, respectively, in the von Mises yield criterion; σ_m is the hydrostatic pressure; f represents the influence of hydrostatic pressure on the yield strength of porous materials. Since F is related to the yield strength $\overline{\sigma_0}$ of the matrix material of the porous material, Equation (1) can be derived in the following form:

$$f'\overline{\sigma}_0 = \sqrt{\frac{1}{2}\left[(\sigma_1-\sigma_2)^2+(\sigma_2-\sigma_3)^2+(\sigma_1-\sigma_3)^2\right]+\left(\frac{\sigma_m}{f}\right)^2} \quad (2)$$

$$f'\overline{\sigma}_0 = \sqrt{\frac{1}{2}\left[(\sigma_1-\sigma_2)^2+(\sigma_2-\sigma_3)^2+(\sigma_1-\sigma_3)^2\right]+\left(\frac{\sigma_m}{f}\right)^2}$$

where f' denotes the ratio of the applied stress on the porous material to the equivalent stress sustained by the fully dense matrix. It is also expressed as a function of the material's relative density. The revised form of the Shima–Oyane model is as follows:

$$F = \frac{1}{f'}\left(\frac{3}{2}\sigma_y\sigma_d+\frac{\sigma_m^2}{f^2}\right)^{0.5}-\sigma_y \quad (3)$$

where F represents the external force; σ_d represents the deviatoric stress tensor; σ_m indicates the hydrostatic pressure; σ_y represents the uniaxial yield stress. In the Shima model, the parameters f and f' directly govern the plastic deformation behavior during the densification of alloy powders. Under uniaxial pressure conditions, the principal stresses satisfy $\sigma_2 = \sigma_3$, $\sigma_m = \sigma_1/3$, from which the corresponding yield condition can be derived:

$$f = \frac{\sqrt{2}}{3}\left(\frac{d\varepsilon_1-d\varepsilon_2}{d\varepsilon_v}\right)^{1/2} \quad (4)$$

$$f' = \frac{\sigma_1(1+1/9f^2)^{1/2}}{\overline{\sigma}_0} \quad (5)$$

where the three principal strains correspond to the principal strain directions ε_1, ε_2, and ε_3. ε_v denotes the volumetric strain, while ρ represents the relative density of the porous material, indicating the fraction of solid matrix present within a unit volume.

In the Shima–Oyane model, the parameters f and f' are critical for characterizing the yield behavior during the densification of alloy powders. The parameter f can be determined through uniaxial compression tests on samples with varying levels of densification, while f' can be obtained by curve fitting the relationship between the yield stress and relative density. Since the yield stress is influenced not only by the relative density but also by the temperature, the relationship between the f' parameter and the temperature can be established through high-temperature uniaxial compression experiments.

2.2. Experiment Procedures for Model Solution and Validation

Since the yield surface in the HIP process is ellipsoidal, two independent experiments are required to determine the corresponding material parameters. In this study, uniaxial compression and interrupted HIP experiments were conducted to characterize the yield surface for the HIP simulation model, as illustrated in Figure 1. The powder used in the HIP process is a commercial-grade material with a particle size distribution ranging from 100 to 150 μm and a nearly spherical morphology, as shown in Figure 2a. The experimental samples were extracted from the preforms produced in the HIP tests described in Figure 2b and subsequently processed according to the uniaxial compression procedure. The samples were compressed by 20% and 40% at 800 °C and 1000 °C to obtain axial strain values corresponding to different densities. After compression, the density of each specimen was measured using the Archimedes drainage method, and the relationship between axial strain and density was established.

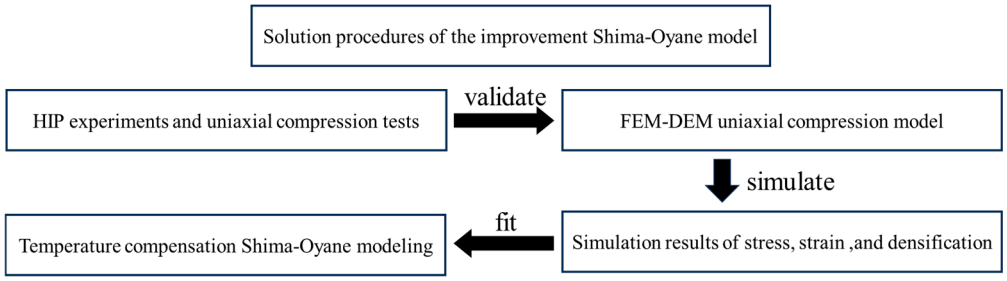


Figure 1. Solution procedures of parameters in the Plasticity model.

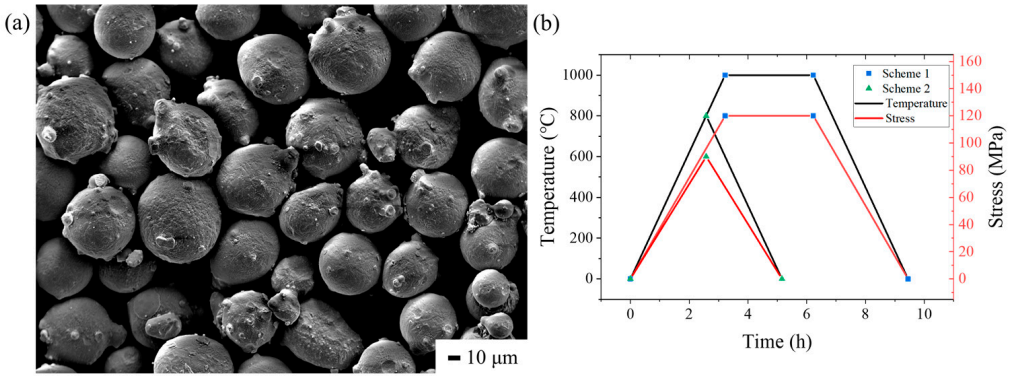


Figure 2. (**a**) Microscopic morphology of the powder; (**b**) HIP experimental process profile.

2.3. FEM-DEM Coupled Procedures for Model Solution and Prediction

The powder particle size used in HIP is on the micrometer scale. Therefore, a smaller numerical model is employed, with sufficiently small grid divisions to ensure the accuracy of the simulation results. Initially, a particle-scale finite element geometric model is constructed in the DEM. The powder material is simplified as spherical, with particle sizes ranging from 20 to 100 μm. The actual particle size distribution of the material is also considered, with the powder diameter following a normal distribution. Figure 3 shows

the flow chart of the coupled thermos–mechanical mesoscopic numerical simulation of the powder HIP process, where each particle is assigned an independent mesh and treated as a distinct individual for calculation. The simulation was conducted at temperatures ranging from 700 °C to 1100 °C under an applied axial pressure of 120 MPa. The inter-particle friction coefficient was set to 0.2.

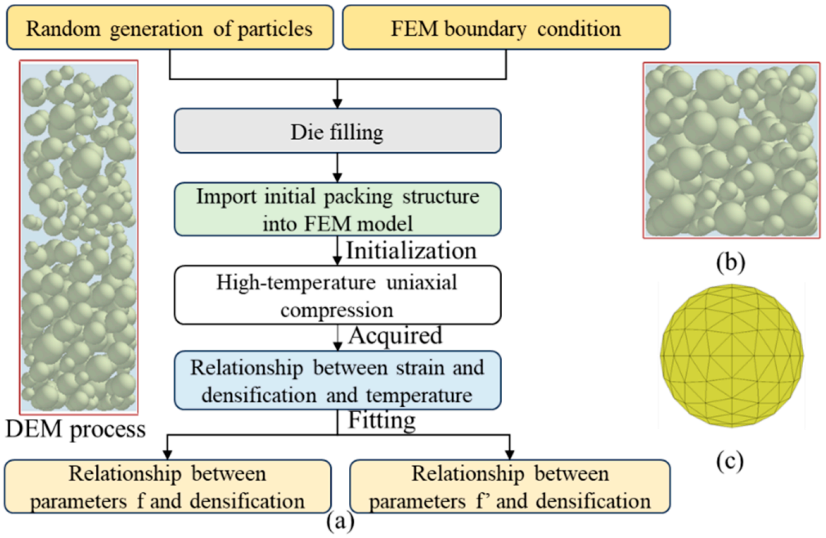


Figure 3. (**a**) Flow chart of mesoscopic numerical simulation of HIP process; (**b**) thermal coupling structure of particle stacking before powder HIP molding; (**c**) mesh division for individual particle.

3. Solution Process of Improved Powder-Yield Model

3.1. Validation of FEM-DEM Coupled Model

Figure 4 shows the true stress–strain curves of a sample with a density of 0.980 at 800 °C and 1100 °C. From the figure, it can be seen that the temperature significantly impacts true stress and yield strength. From the true stress–strain data, it can be derived that when the compression temperature is 1100 °C, the yield stress of Inconel 625 alloy is 113.648 MPa and 139.570 MPa for deformation amounts of 20% and 40%, respectively. When the compression temperature is 800 °C, the yield stress of the Inconel 625 alloy is 312.925 MPa. The densification of each sample after uniaxial compression was also measured. Under compression conditions of 1100 °C and 0.01 s^{-1}, the densification was 0.985 after 20% compression and 0.991 after a 40% compression. Under compression conditions of 800 °C and 0.01 s^{-1}, the densification was 0.982 after a 20% compression.

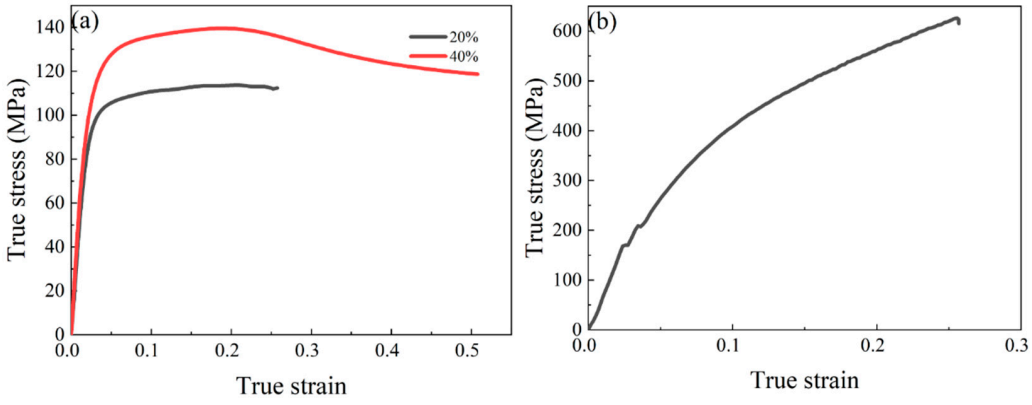


Figure 4. Stress–strain curves of samples with a densification of 0.980 at different temperatures: (**a**) 1100 °C; (**b**) 800 °C.

As shown in Table 1, a comparison of the strain increase corresponding to the same densification increase is presented under the same initial densification. According to Table 1, the error between experimental and simulated strain increments is within 5% for different densification increments, indicating that mesoscopic powder particle-scale simulations can effectively predict strain increments at different densification levels.

Table 1. Comparison of axial strain increments between simulated and experimental results at the same densification increments.

Initial Density	Temperature	Density Increment	Strain		Relative Error (%)
			Experimental Results	Simulation Results	
0.980	1100 °C	0.005	0.26	0.25	4.7
0.980	1100 °C	0.013	0.51	0.53	3.7
0.980	800 °C	0.023	0.26	0.27	4.3

Table 2 compares the yield stress obtained experimentally and through simulation at the same densification. The table shows that the yield stress obtained experimentally and the yield stress obtained through simulation differ only slightly, with an error of about 5%. This indicates that mesoscopic particle-scale simulations can effectively predict the yield strength of the Inconel 625 alloy at different densifications and temperatures.

Table 2. Comparison of experimental and simulated yield stresses at the same uniform density.

Initial Density	Temperature (°C)	Yield Stress		Relative Error (%)
		Experimental Results (MPa)	Simulation Results (MPa)	
0.985	1100	113.6	108.8	4.2
0.990	1100	139.6	132.5	5.1
0.982	800	625.9	602.0	3.8

3.2. Compensation of Temperature Influence on Shima–Oyane Model

Through the validated FEM-DEM coupled high-temperature uniaxial compression model, the strain and density data of the powder at various temperatures were obtained. Figure 5a illustrates the relationship between axial strain and density during the uniaxial compression process. At lower densities, the axial strain remains close to zero, indicating that particle movement and rearrangement dominate at this stage, with minimal plastic deformation of the powder particles. As the compression progresses, the plastic deformation becomes more pronounced. Due to the softening effect at elevated temperatures, the axial strain increases more rapidly with rising temperature.

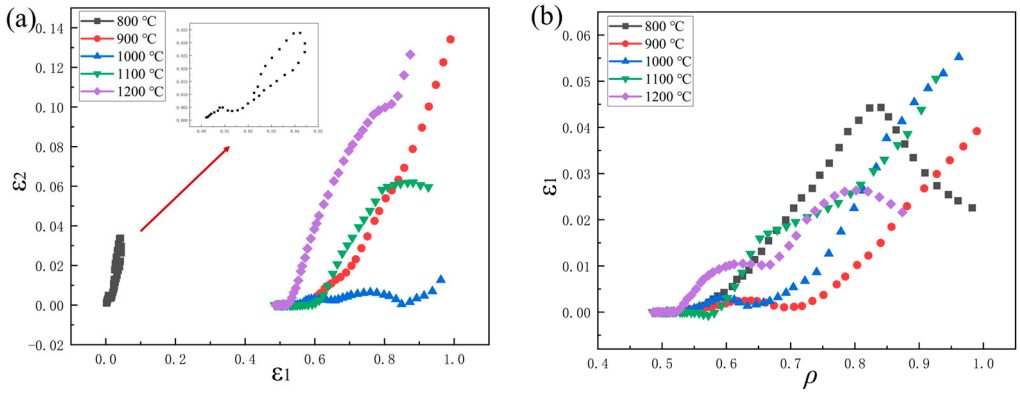


Figure 5. The relationships of axial strain with (**a**) the relative density and (**b**) the radial strain.

Figure 5b presents the relationship between axial strain and radial strain during uniaxial compression. At the initial stage and under low-temperature conditions, the radial strain is nearly zero, suggesting that the plastic deformation is limited and the radial expansion is suppressed. However, at higher temperatures, the plastic deformation occurs more readily due to thermal softening. As the compression continues, the radial strain at low temperatures exhibits a rapid increase, while at high temperatures, it increases gradually and smoothly. This behavior may be associated with thermally activated recovery and recrystallization processes, which are not discussed in detail in this study.

As shown in Figure 6, the value of f can be calculated by substituting the experimentally verified strain and density data obtained from high-temperature uniaxial compression tests at different temperatures into Formula (4). As can be seen from the figure, the f values are relatively scattered, and they overlap between different temperatures, without showing any temperature dependence.

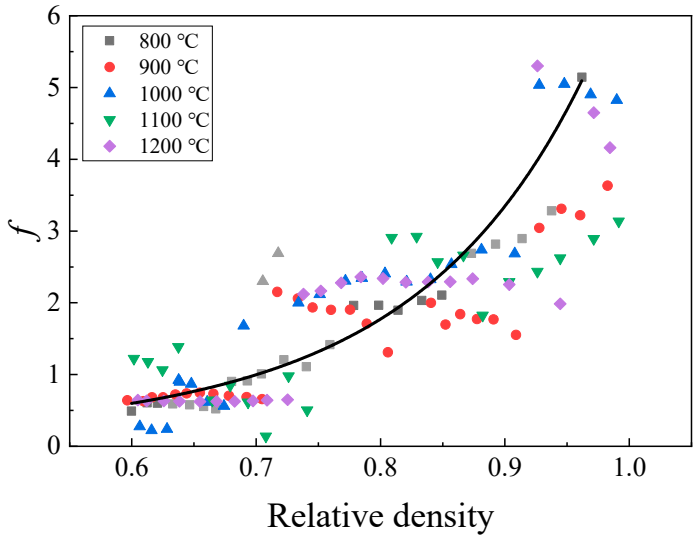


Figure 6. Variation in parameter f with relative density.

The parameters f' and f are the material parameters of the powder, which are fitted through the following two formulas, which simplify both f and f' into functions related to density. The fitting results of parameter f are shown in Figure 6.

$$f\prime = (b_1 + b_2]\rho^{b_3})^{b_4} \tag{6}$$

$$f = (q_1 + q_2\rho^{q_3})^{q_4} \tag{7}$$

where b_1, b_2, b_3, and b_4 are the material constants related to temperature; q_1, q_2, q_3, and q_4 are the material constants. The fitting result is as follows:

$$f = \left(0.91632 + 0.17049\ ]\rho^{1.99964}\right)^{22.79806} \tag{8}$$

The yield strength of the fully dense Inconel 625 alloy matrix is 500 MPa. Combining the values of σ_1 at different densities and temperatures, the corresponding values f for different densifications are calculated and the parameters f' can be determined by substituting into Equation (8), as shown in Figure 7. Since the parameter f' is related to stress and stress is affected by temperature, for powders with the same densification, higher temperature results in lower stress. Thus, the parameter f' also decreases. From the figure, it can also be seen that at different temperatures, the parameter f' increases with densification, and as

densification increases, the rate of increase accelerates. Therefore, the calculated parameter f' is fitted separately for each temperature, with the fitting results shown in Equation (9).

$$\begin{cases} f'_{T=800} = (0.99801 + 0.00552\,]\rho^{9.07827})^{104.74863} \\ f'_{T=900} = (0.98668 + 0.01521\,]\rho^{4.4382})^{51.48709} \\ f'_{T=1000} = (0.96541 + 0.02242\,]\rho^{3.83392})^{28.93245} \\ f'_{T=1100} = (0.98574 + 0.00858\,]\rho^{6.74518})^{86.32917} \\ f'_{T=1200} = (0.93754 + 0.02054\,]\rho^{3.97408})^{31.99983} \end{cases} \quad (9)$$

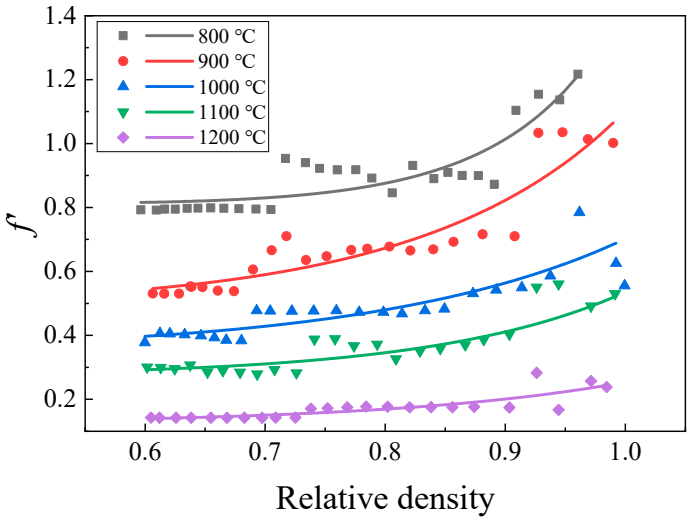


Figure 7. Variation in parameter f' with relative density.

The most suitable temperature-dependent expression functions for the four material parameters are found, and the material constants of the Inconel 625 alloy are expressed as temperature-dependent functions.

$$\begin{cases} b_1 = C_1 + C_2T^2 + C_3T^4 + C_4T^6 \\ b_2^{-1} = D_1 + D_2T + D_3T^2 + D_4T^3 \\ b_3 = E_1 + E_2T^2\ln T + E_3T^{2.5} + E_4T^3 \\ b_4^2 = G_1 + G_2T + G_3T^2 + G_4T^3 \end{cases} \quad (10)$$

The variation trends of the material constants b_1, b_2, b_3, and b_4 after the function fitting are shown in Figure 8.

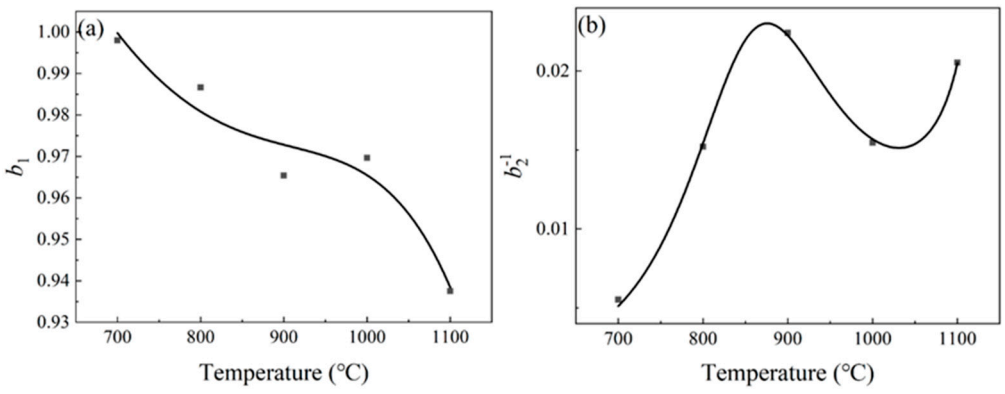


Figure 8. *Cont.*

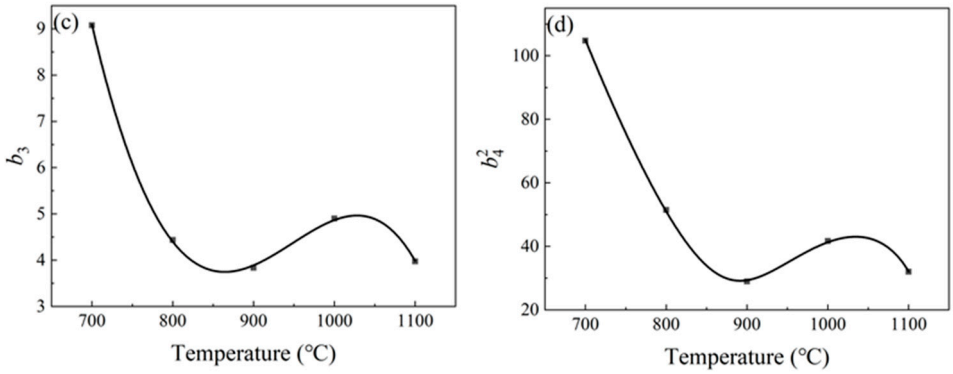


Figure 8. Fitting of material constants (**a**) b_1, (**b**) b_2, (**c**) b_3, and (**d**) b_4 to temperature.

Based on the above formulas, the coefficients are determined through nonlinear function fitting using the Origin 2019b software, as shown in Table 3.

Table 3. Correlation coefficients of Inconel 625 alloy b_1, b_2, b_3, and b_4 fitting functions.

	b_1		b_2		b_3		b_4
C_1	1.25004	D_1	10,295.841	E_1	164.52288	G_1	601,825.6
C_2	-9.42466×10^{-7}	D_2	−32.66279	E_2	−0.00721	G_2	−1891.7101
C_3	1.09527×10^{-12}	D_3	0.03449	E_3	0.00024	G_3	1.97538
C_4	-4.37362×10^{-19}	D_4	-1.20587×10^{-5}	E_4	-2.7258×10^{-6}	G_4	−0.00068

3.3. Construction of Stress–Strain–Temperature–Density Relationships

Based on the obtained parameters at various densities and temperatures, a yield stress map for the nickel-based alloy was constructed, as shown in Figure 9. In this figure, the contour lines represent variations in the yield strength with the temperature at a given density, and the labeled values indicate the corresponding yield stresses. The color gradient visually illustrates the yield stress distribution. As observed, the yield stress decreases with the increasing temperature, reaching a minimum of 52.087 MPa at 1200 °C. Conversely, as the density increases, the yield strength of the material also rises. Thus, the yield strength is jointly influenced by both the temperature and the density, exhibiting a nonlinear relationship. Although a higher density contributes to an increase in the yield stress, the dominant factor influencing its variation is the reduction caused by elevated temperatures. At a constant temperature, the maximum variation in the yield stress is 101.214 MPa, while at a constant density, the maximum variation is 244.515 MPa.

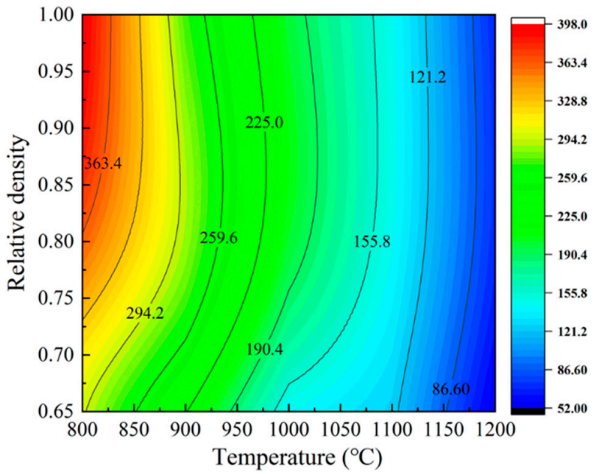


Figure 9. Yield strength as a function of temperature and densification.

4. Predication of Powder Densification Behaviors and Validation Evaluation

4.1. Presentation of Stress–Strain–Temperature–Density Relationships by Solved Model

4.1.1. Macroscopic Analysis of the Experimental Results

During the powder HIP process, powder densification is mainly driven by the deformation of the casing. Uniform deformation of the casing results in a uniformly densified final part. However, suppose the local deformation in the casing is too large or too small; in that case, it can not only lead to a casing rupture but also cause localized densification and non-uniformity in the formed part. Therefore, the deformation of the casing directly affects the total performance of the final part. The green bodies obtained from the two different HIP processes shown in Figure 2 are illustrated in Figure 10. The figure shows that after holding at 1000 °C and 120 MPa for 180 min under process scheme 1, the shrinkage deformation of the casing in the cylindrical part is noticeably greater than that of the cylindrical part formed with process scheme 2. To quantitatively compare the casing shrinkage deformation under the two process schemes, axial and radial measurements of the casing were performed. After measurements, it was found that the casing processed under process scheme 1 experienced an axial shrinkage of 13.24 mm and a radial shrinkage of 12.50 mm. After processing with process scheme 2, the casing experienced an axial shrinkage of 5.32 mm and a radial shrinkage of 4.46 mm. It is evident that the process parameters significantly affect the casing shrinkage and play a decisive role in the powder densification process.



Figure 10. Comparison of two post-HIP program capsule sets.

During the HIP process, powder densification is primarily driven by the deformation of the encapsulating structure. The degree of densification within the powder compact closely correlates with the extent of capsule deformation. Figure 11 provides a comparative visualization of the central axial cross-sections obtained from experimental observation and numerical simulation. As illustrated, the deformation profiles of the truncated capsule in the central axial direction are highly consistent, indicating good agreement between the model and experimental results. To further evaluate the fidelity of the simulation, two characteristic lines were selected: L1, extending diagonally from the powder corner to the center point, and L2, corresponding to the axis of symmetry through the center. Three feature nodes were designated along each line—A1, A2, and A3 on L1, and B4 and B5 on L2—with A3 located precisely at the intersection of L1 and L2, at the powder's geometric center. Samples with dimensions of ø10 mm × 12 mm were extracted from each feature location. The sample densities were determined via the Archimedes drainage method, with each mass measurement repeated multiple times and averaged to enhance the measurement reliability. The measured densities were quantitatively compared with the

simulated results at the corresponding nodes. The close match between the experimental and simulated densities validates the predictive capability of the simulation model.

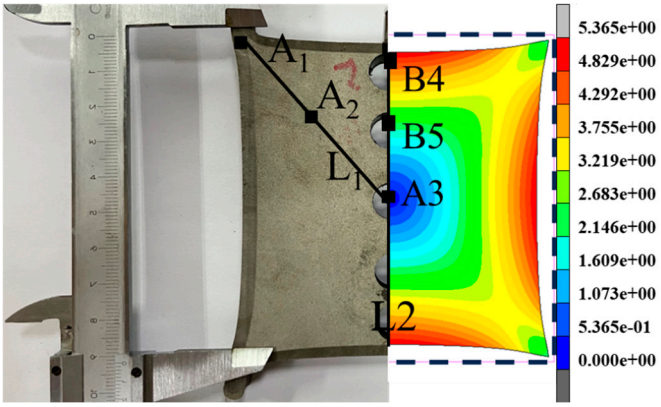


Figure 11. Macro-deformation comparison.

4.1.2. Evolution of the Relative Density

Figure 12 illustrates the density evolution of five feature nodes during the HIP process, which consists of three stages: heating and pressurization, holding and pressure maintenance, and cooling and depressurization. In the initial stage of the HIP, the density at each node decreases due to the thermal expansion of the powder, while the applied pressure is insufficient to counteract this expansion, resulting in a temporary increase in volume. However, this stage is brief, and the reduction in density is minimal compared to the overall increase. As the HIP process progresses, the temperature and pressure rise. At 7000 s, the density at each node begins to increase rapidly. The applied pressure becomes sufficient to exceed the powder's yield strength, causing shrinkage and deformation. Since the initial powder packing is relatively loose, a significant plastic deformation occurs, leading to a more compact internal arrangement. For feature line L1, nodes A1, A2, and A3 exhibit similar density growth patterns, with densities steadily increasing after the initial HIP stage. The final densities of A2 and A3 reach approximately 0.97, higher than A1, due to A2 and A3 being closer to the center of the powder, while A1 is affected by its position at the edge, near the corner and end caps, resulting in a lower density. Nodes B4, B5, and A3 along line L2 show similar trends, with their density curves largely coinciding. After an initial reduction, the density increases steadily, but the rate of increase slows during the later holding stage as densification approaches saturation. At this point, the densification is primarily driven by diffusion and creep, and the final density reaches approximately 0.97.

4.1.3. Microstructure of HIP Sample

As shown in Figure 13, the microstructure of the billet, sampled from the center cross-section at a temperature of 1100 °C, a pressure of 120 MPa, and a holding time of 3 h, exhibits a density of 0.980. In comparison, Figure 12 shows that the simulated density at the center of the cylindrical part reaches 0.972. The minimal deviation between the simulated and experimental values confirms the accuracy of the simulation results. Figure 13 visually presents the microstructural features, showing a markedly more compact arrangement of powder particles. The pores are nearly eliminated, and the particles exhibit substantial plastic deformation, indicating effective densification during the HIP process. The billet was processed by HIP, a technique that applies high temperature and isostatic gas pressure to densify materials and eliminate internal pores. After HIP, the density of the powder material has substantially improved, with some regions showing almost complete elimination of porosity. However, original particle boundaries remain visible, and distinct grain boundary

features can still be observed, as shown in the yellow circle. This indicates that, despite the applied process parameters, some powder particles did not fully fuse during HIP. The causes of this incomplete fusion are complex and are beyond the scope of this paper.

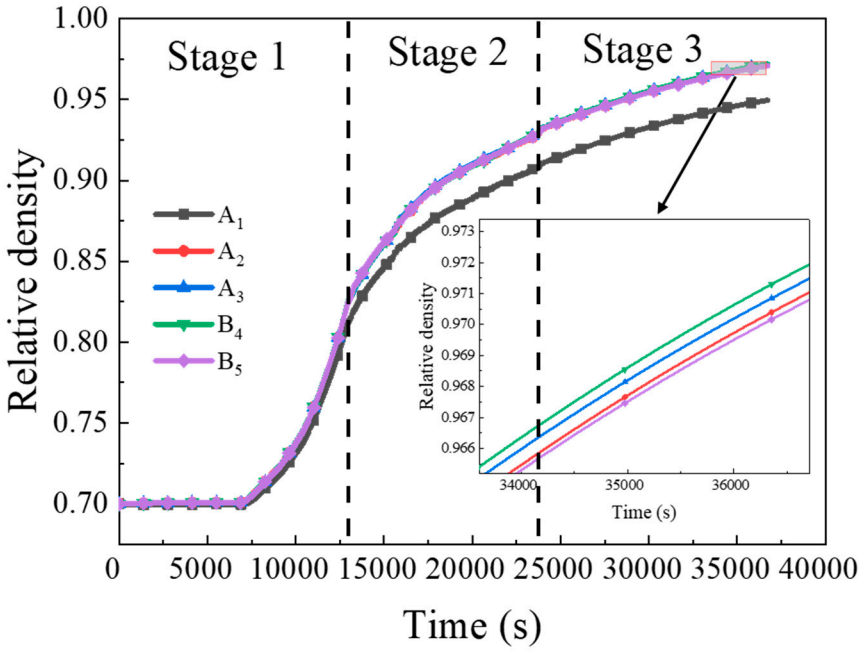


Figure 12. Evolution of the relative density of different feature points over time.

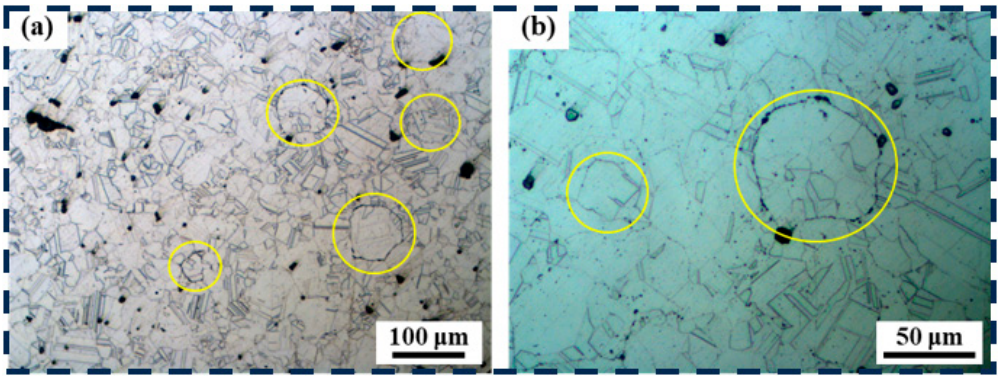


Figure 13. Microstructure of HIP parts: (**a**) 100X and (**b**) 200X.

4.2. Validation Evaluation of Improved Powder-Yield Model

The results comparing the densities from the experimental and numerical simulations are shown in Figure 14. It can be observed that, under the same parameter conditions, the densities at each feature location of the cylinders formed by HIP are similar to the results of the numerical simulations, with the densities of the five feature nodes all exceeding 0.95. Specifically, due to the influence of the capsule's edges and corners, the experimentally obtained cylinder has the lowest density of 0.96 at feature node A1, while the densities at the other four feature nodes are around 0.98. The density variation between the nodes is no more than 0.02, indicating good homogeneity of the HIPed powder. As shown in Figure 14, the relative errors between the experimental and simulation results for the five feature points are 1.07%, 1.15%, 1.35%, 1.09%, and 1.21%, respectively, all within 2%. Overall, the simulated densities are slightly lower than the experimental densities, which can be attributed to the nature of the macroscopic simulation, where the powder is treated as a continuous porous medium. This differs from the discrete particle nature of the HIP process, which ignores the effects of powder particle rearrangement during the initial

stage and the diffusion creep at high temperatures during the final stage. Nevertheless, the comparison of the numerical simulation and experimental results for the macroscopic deformation and densification at feature locations shows that the numerical simulation method used in this study provides an accurate prediction of the densification behavior of powders during powder HIP.

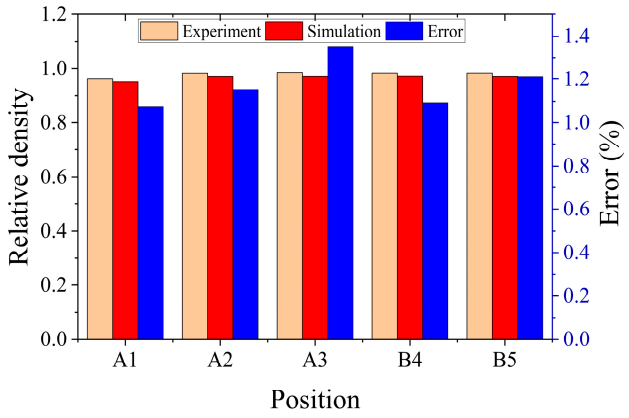


Figure 14. Comparison of simulation results with experimental results.

5. Conclusions

Based on the DEM theory, a mesoscopic particle-scale numerical model of the powder HIP was constructed. Based on the numerical model, the stress and strain parameters of the particles in the forming process under different temperature and pressure conditions were extracted and characterized as a function of the degree of densification. Uniaxial compression experiments verified the above parameters' HIPed samples at different temperatures. Then, a temperature-dependent Shima–Oyane model based on the validation parameters was developed. Key findings were as follows:

The parameters relating to the stress, strain, and densification at different temperatures and pressures were obtained based on the mesoscopic particle-scale model. The strain increments and stress at different densification levels were compared by conducting uniaxial compression experiments on samples at different temperatures. The relative error between the experimental and simulation results was within 5.1%. The mesoscopic particle-scale simulations accurately determined the parameters related to the stress, strain, and densification.

The parameters relating to the stress, strain increments, and densification at different temperatures (800–1100 °C) were obtained based on the mesoscopic particle-scale model. A temperature-compensated Shima–Oyane model was developed. Based on the parameters f and f', a three-dimensional relationship graph illustrating the correlation between the yield stress, density, and temperature was constructed. To validate the proposed temperature-compensated Shima–Oyane model, the deformation behavior and density distribution of the powder components formed via the HIP were investigated. The results showed that the simulated final deformation closely matched the experimental observations, and the relative errors in the predicted densities across different regions were within 2%. These findings confirm that the constructed macroscopic finite-element model can reliably predict the densification behavior during the HIP process.

Although this study presents a mesoscopic–macroscopic coupled analysis of the HIP forming process under various parameter conditions, it should be acknowledged that the Shima–Oyane model is limited in capturing the fundamental densification mechanisms of hot isostatic pressing, such as diffusional creep and grain boundary diffusion. Physically based creep models are better suited to represent the microstructural deformation

mechanisms that dominate during the HIP process. Additionally, the current DEM model provides a foundation for particle-scale studies of the densification process during hot isostatic pressing. These aspects will be the primary focus of the authors' future work.

Author Contributions: Conceptualization, G.Q. and W.R.; Methodology, G.Q. and W.R.; Validation, Q.J., Y.Y. and Y.Z.; Formal Analysis, W.D.; Investigation, Y.Z.; Resources, G.Q.; Data Curation, W.R., W.D., Q.J. and Y.Y.; Writing—Original Draft Preparation, W.R.; Writing—Review & Editing, G.Q. and W.R.; Visualization, W.R. and W.D.; Supervision, G.Q.; Funding Acquisition, G.Q. All authors have read and agreed to the published version of the manuscript.

Funding: The authors are grateful for the supports from National Natural Science Foundation of China (52175287) and Chongqing Natural Science Foundation General Project (CSTB2022NSCQ-MSX0593).

Data Availability Statement: The original contributions presented in this study are included in the article. Further inquiries can be directed to the corresponding author.

Conflicts of Interest: Authors Weiwei Dai and Qian Jiang were employed by COSCO Shipping Marine Equipment & Spares (Nanjing) Co., Ltd. Author Guozheng Quan was a part-time employee of COSCO Shipping Marine Equipment & Spares (Nanjing) Co., Ltd. The remaining authors declare that the research was conducted in the absence of any commercial or financial relationships that could be construed as a potential conflict of interest.

References

1. Boris, B.I.; Genrikh, G.S.; Oleg, F.C. Prospect of HIP application in aerospace and power plant industry. In Proceedings of the International Conference on Hot Isostatic Pressing, Andover, MA, USA, 20–22 May 1996.
2. Atkinson, H.V.; Davies, S. Fundamental aspects of hot isostatic pressing: An overview. *Metall. Mater. Trans. A* **2000**, *31*, 2981–3000. [CrossRef]
3. Zhang, H.; Wang, A.; Wen, Z.; Yue, Z.; Zhang, C. Effects of Hot Isostatic Pressing (HIP) on Microstructure and Mechanical Properties of K403 Nickel-Based Superalloy. *High Temp. Mater. Process.* **2016**, *35*, 463–471. [CrossRef]
4. ElRakayby, H.; Kim, K. Effect of glass container encapsulation on deformation and densification behavior of metal powders during hot isostatic pressing. *Int. J. Mater. Form.* **2017**, *11*, 517–525. [CrossRef]
5. Semiatin, S.L. An Overview of the Thermomechanical Processing of α/β Titanium Alloys: Current Status and Future Research Opportunities. *Metall. Mater. Trans. A* **2020**, *51*, 2593–2625. [CrossRef]
6. Kim, H.S. Densification mechanisms during hot isostatic pressing of stainless steel powder compacts. *J. Mater. Process. Technol.* **2002**, *123*, 319–322. [CrossRef]
7. Xue, Y.; Lang, L.; Bu, G.; Li, L. Densification Modeling of Titanium Alloy Powder during Hot Isostatic Pressing. *Sci. Sinter.* **2011**, *43*, 247–260. [CrossRef]
8. Abdelhafeez, A.; Essa, K. Influences of Powder Compaction Constitutive Models on the Finite Element Simulation of Hot Isostatic Pressing. *Procedia CIRP* **2016**, *55*, 188–193. [CrossRef]
9. Wei, Q.S.; Xue, P.J.; Liu, G.C.; Lu, H.; Huang, J.; Shi, Y.S. Simulation and verification of near-net shaping a complex-shaped turbine disc by hot isostatic pressing process. *Int. J. Adv. Manuf. Technol.* **2014**, *74*, 1667–1677. [CrossRef]
10. Zhou, S.; Song, B.; Xue, P.; Cai, C.; Liu, J.; Shi, Y. Numerical simulation and experimental investigation on densification, shape deformation, and stress distribution of Ti6Al4V compacts during hot isostatic pressing. *Int. J. Adv. Manuf. Technol.* **2017**, *88*, 19–31. [CrossRef]
11. Bu, G.L.; Lang, L.H.; Wang, G.; Song, Y.; Xu, Q.Y. Forming and Simulation of Titanium Alloy Ti-6Al-4V by Hot Isostatic Pressing. *Adv. Mater. Res.* **2013**, *848*, 50–54. [CrossRef]
12. Wang, M.; Yin, Y.J.; Zhou, J.X.; Ji, X.Y.; Nan, H.; Xue, P.J.; Shi, Y.S. A multi-scale study of Inconel 625 powders HIP process and construction of HIP maps. *Int. J. Adv. Manuf. Technol.* **2017**, *90*, 3055–3066. [CrossRef]
13. Liu, G.C.; Shi, Y.S.; Wei, Q.S.; Wang, J.W. Finite Element Analysis of Pressure Influence on Densification of Titanium Alloy Powder under Hot Isostatic Pressing. *Key Eng. Mater.* **2010**, *450*, 206–209. [CrossRef]
14. Geindreau, C.; Bouvard, D.; Doremus, P. Constitutive behaviour of metal powder during hot forming. Part I: Experimental investigation with lead powder as a simulation material. *Eur. J. Mech. A Solids* **1999**, *18*, 581–596. [CrossRef]
15. Van Nguyen, C.; Bezold, A.; Broeckmann, C. Anisotropic shrinkage during hip of encapsulated powder. *J. Mater. Process. Technol.* **2015**, *226*, 134–145. [CrossRef]
16. Han, P.; An, X.Z.; Wang, D.F.; Fu, H.T.; Yang, X.H.; Zhang, H.; Zou, Z.S. MPFEM simulation of compaction densification behavior of Fe-Al composite powders with different size ratios. *J. Alloys Compd.* **2018**, *741*, 473–481. [CrossRef]

17. Wang, B.; Pan, K.J.; Gao, S.; Wu, S.X.; Zhao, C.; Luo, X.; Peng, Q.; Sun, M.H.; Li, D.D.; Li, N.; et al. Synergistic densification mechanism of irregular Ti powder during CIP: 3D MPFEM simulation with real-shape particles. *Mater. Des.* **2024**, *246*, 113368. [CrossRef]
18. Xu, L.; Wang, Y.; Li, C.; Ji, G.; Mi, G. MPFEM simulation on hot-pressing densification process of SiC particle/6061Al composite powders. *J. Phys. Chem. Solids* **2021**, *159*, 110259. [CrossRef]
19. Zhang, W.; Yuan, C.; Xiao, W.; Gong, X.; Hai, B.; Chen, R.; Zhou, J. MPFEM investigation on densification and mechanical structures during ferrous powder compaction. *Adv. Powder Technol.* **2024**, *35*, 104700. [CrossRef]
20. Zou, Y.; An, X.; Zou, R. Investigation of densification behavior of tungsten powders during hot isostatic pressing with a 3D multi-particle FEM approach. *Powder Technol.* **2020**, *361*, 297–305. [CrossRef]
21. Harthong, B.; Imbault, D.; Dorémus, P. The study of relations between loading history and yield surfaces in powder materials using discrete finite element simulations. *J. Mech. Phys. Solids* **2012**, *60*, 784–801. [CrossRef]
22. Loidolt, P.; Ulz, M.H.; Khinast, J. Modeling yield properties of compacted powder using a multi-particle finite element model with cohesive contacts. *Powder Technol.* **2018**, *336*, 426–440. [CrossRef]
23. Güner, F.; Sofuoglu, H.; Cora, Ö.N. An investigation of contact interactions in powder compaction process through variable friction models. *Tribol. Int.* **2016**, *96*, 1–10. [CrossRef]
24. Xin, X.J.; Jayaraman, P.; Jiang, G.; Wagoner, R.H.; Daehn, G.S. Explicit finite element method simulation of consolidation of monolithic and composite powders. *Met. Mater. Trans. A* **2002**, *33*, 2649–2658. [CrossRef]
25. Zhou, J.; Xu, H.; Zhu, C.; Wang, B.; Liu, K. Comparisons Between 2D and 3D MPFEM Simulations in Modeling Uniaxial High Velocity Compaction Behaviors of Ti-6Al-4V Powder. *Arch. Metall. Mater.* **2022**, *67*, 57–65. [CrossRef]
26. Zhou, J.; Zhu, C.; Zhang, W.; Ai, W.; Zhang, X.; Liu, K. Experimental and 3D MPFEM simulation study on the green density of Ti-6Al-4V powder compact during uniaxial high velocity compaction. *J. Alloys Compd.* **2020**, *817*, 153226. [CrossRef]
27. Elguezabal, B.; Martínez-Esnaola, J.; Soler, R.; Paños, E.; Alkorta, J. A multiscale material model for metallic powder compaction during hot isostatic pressing. *Powder Technol.* **2023**, *425*, 118599. [CrossRef]
28. Li, M.; Lim, C.V.S.; Zou, R.; An, X.; Wang, D. Multi-particle FEM modeling on hot isostatic pressing of Ti6Al4V powders. *Int. J. Mech. Sci.* **2021**, *196*, 106288. [CrossRef]
29. Li, M.; Jia, Q.; Li, C.; Guo, Q.; An, X.; Zou, Q.; Zhou, X.; Fu, H.; Zhang, H.; Yang, X.; et al. 3D particulate-scale numerical investigation on hot isostatic pressing of W-Cu composites. *Powder Technol.* **2023**, *415*, 118150. [CrossRef]
30. Oyane, M.; Shima, S.; Kono, Y. Thoery of Plasticity for Porous Metals. *Bull. JSME* **1973**, *16*, 1254–1262. [CrossRef]
31. Shima, S.; Oyane, M. Plasticity theory for porous metals. *Int. J. Mech. Sci.* **1976**, *18*, 285–291. [CrossRef]

Disclaimer/Publisher's Note: The statements, opinions and data contained in all publications are solely those of the individual author(s) and contributor(s) and not of MDPI and/or the editor(s). MDPI and/or the editor(s) disclaim responsibility for any injury to people or property resulting from any ideas, methods, instructions or products referred to in the content.